nanomaterials

MDPI

Article

Synergistic Piezo-Photocatalysis of BiOCl/$NaNbO_3$ Heterojunction Piezoelectric Composite for High-Efficient Organic Pollutant Degradation

Li Li [1], Wenjun Cao [1], Jiahao Yao [1], Wei Liu [1], Feng Li [2,*] and Chunchang Wang [1,*]

[1] Laboratory of Dielectric Functional Materials, School of Materials Science & Engineering, Anhui University, Hefei 230601, China; b20101003@stu.ahu.edu.cn (L.L.); caowenjun1206@126.com (W.C.); yjh1074457726@163.com (J.Y.); b20301114@stu.ahu.edu.cn (W.L.)

[2] Information Materials and Intelligent Sensing Laboratory of Anhui Province, Institutes of Physical Science and Information Technology, Anhui University, Hefei 230601, China

* Correspondence: fengli@ahu.edu.cn (F.L.); ccwang@ahu.edu.cn (C.W.)

Abstract: Piezo-photocatalytic technique is a new-emerging strategy to alleviate photoinduced charge recombination and thus enhance catalytic performance. The heterojunction construction engineering is a powerful approach to improve photocatalytic performance. Herein, the BiOCl/$NaNbO_3$ with different molar ratios piezoelectric composites were successfully synthesized by hydrothermal methods. The piezo/photodegradation rate (k value) of Rhodamine B (RhB) for BiOCl/$NaNbO_3$ (BN-3, 0.0192 min^{-1}) is 2.2 and 5.2 times higher than that of BiOCl (0.0089 min^{-1}) and $NaNbO_3$ (0.0037 min^{-1}), respectively. The enhanced performance of BN-3 composite can be attributed to the heterojunction construction between BiOCl and $NaNbO_3$. In addition, the piezo/photodecomposition ratio of RhB for BN-3 (87.4%) is 8.8 and 2.2 times higher than that of piezocatalysis (9.9%) and photocatalysis (40.4%), respectively. We further investigated the mechanism of piezocatalysis, photocatalysis, and their synergy effect of BN-3 composite. This study favors an in-depth understanding of piezo-photocatalysis, providing a new strategy to improve the environmental pollutant remediation efficiency of piezoelectric composites.

Keywords: BiOCl/$NaNbO_3$; heterojunction; piezocatalysis; photocatalysis; degradation

Citation: Li, L.; Cao, W.; Yao, J.; Liu, W.; Li, F.; Wang, C. Synergistic Piezo-Photocatalysis of BiOCl/$NaNbO_3$ Heterojunction Piezoelectric Composite for High-Efficient Organic Pollutant Degradation. *Nanomaterials* **2022**, *12*, 353. https://doi.org/10.3390/nano12030353

Academic Editor: Dong-Joo Kim

Received: 30 December 2021
Accepted: 20 January 2022
Published: 22 January 2022

1. Introduction

There is increasing social concern over the current energy and environmental issues, especially wastewater pollution (originating from rapid industrial development), which poses a direct threat to human health [1,2]. Researchers are seeking effective, cost-efficient, stable, and safe ways to degrade and remove hazardous compounds in water. Semiconductor photocatalysis is one of the prominent strategies, not only converting sustainable solar energy into hydrogen energy but also utilizing visible light to degrade organic pollutants. A large number of semiconductor photocatalysts and their composites have been reported to improve the water splitting or pollutant degradation performance, such as ZnO and WO_3 [3–5]. Among the various semiconductors, bismuth oxychloride (BiOCl) as a p-type bismuth oxyhalides semiconductor has an open layered structure composing of $[Bi_2O_2]^{2+}$ layers sandwiched between $[Cl_2]^{2-}$ plates, which can facilitate the separation of photo-produced electrons and holes due to the more space to polarize the atoms and orbitals involved [6]. However, BiOCl is limited by its wide band gap (~3.4 eV), representing favorable photocatalytic performance only under ultraviolet light irradiation. Therefore, heterojunction–construction engineering is one of the most powerful strategies to achieve a broader photoresponse and improved photocatalytic activity by constructing heterostructured BiOCl photocatalysts [7–9].

In addition to photocatalysis, piezoelectric catalysis is also an efficient and environmentally friendly dye degradation method [10–12]. Vibration is one of the most common

sources of energy in our environment. In piezoelectric catalysis, mechanical vibration generates an electric charge on the surface of the piezoelectric catalyst through the piezoelectric effect, which in turn reacts with the dye molecules, leading to the decomposition of the dye [13,14]. Combining with photocatalysis, piezoelectric materials possess the ability to reduce the carrier recombination rate due to the existence of an internal piezoelectric field in piezoelectric materials. In past decades, perovskite niobates, including $NaNbO_3$, have attracted intensive attention because of their nonlinear optics, ionic conductive, piezoelectric, and photocatalytic properties [15–17]. In addition, the piezo-photocatalysis and pyroelectric catalysis of $NaNbO_3$ have been thoroughly studied in recent years. For example, Jia's group has found that $NaNbO_3$ nanofibers possess a highly efficient piezoelectrically and pyroelectrically bi-catalysis for decomposition of organic dye [18]. It is worth noting that BiOCl is a piezoelectric material with piezocatalytic activity in response to ultrasound. Jia's group have also reported that BiOCl shows highly efficient dye wastewater decomposition under the condition of light (300 W Xenon lamp) and ultrasound (120 W, 40 kHz) together, which is much greater than that of only with light or only with ultrasound, respectively [19]. However, there are not any reports for piezo-photocatalysis of BiOCl/$NaNbO_3$ heterojunction piezoelectric composite. Therefore, it is necessary to explore the mechanism of BiOCl/$NaNbO_3$ piezoelectric composite for enhancing degradation efficiency by using the synergistic effect of piezoelectric catalysis and photocatalysis.

In this work, the BiOCl/$NaNbO_3$ piezoelectric composites were prepared by the hydrothermal method. The polarization electric field hysteresis loop (P-E) and electric-field-induced strain (S-E) curves confirm the BiOCl/$NaNbO_3$ composite has good ferroelectric and piezoelectric properties. The catalytic performance of BiOCl/$NaNbO_3$ piezoelectric composite was remarkably enhanced by the heterojunction construction and the synergy effect of piezocatalysis and photocatalysis, which greatly promote the separation of electron-hole pairs under electric field.

2. Materials and Methods

2.1. Materials Fabrication

2.1.1. Synthesis of $NaNbO_3$

The $NaNbO_3$ powder was prepared by the hydrothermal method. Briefly, 1 g Nb_2O_5 was added into 30 mL sodium hydroxide (NaOH, 10 M) aqueous solution and stirred for 2 h. Then, transferred above solution into a 50 mL Teflon-lined autoclave and reacted at 180 °C for 48 h. The precipitate was washed thoroughly and dried at 80 °C.

2.1.2. Synthesis of BiOCl

In brief, 5 mmol bismuth nitrate ($Bi(NO_3)_3{\cdot}5H_2O$, 99.5%) and 5 mmol potassium chloride (KCl) were added into 30 mL deionized water (DI water) and stirred for 0.5 h. Then, the above solution was transferred into a 50 mL Teflon-lined autoclave and heated at 180 °C for 12 h. The precipitate was washed thoroughly and dried at 80 °C.

2.1.3. Synthesis of BiOCl/$NaNbO_3$ Composites

Different contents (1, 2, 3, 4 mmol) of $NaNbO_3$ (prepared in 2.1.1) were added into the 30 mL DI water and stirred for 0.5 h, and then, 5 mmol $Bi(NO_3)_3{\cdot}5H_2O$ and 5 mmol KCl were added into the solution and stirred for another 0.5 h. The above solution was transferred into a 50 mL Teflon-lined autoclave and reacted at 180 °C for 12 h. The corresponding composites were named as BN-1, BN-2, BN-3, BN-4.

2.2. Photocatalytic Performance Experiment

The piezo/photocatalytic activities were evaluated by the degradation of RhB under UV–vis light irradiation and ultrasound. The 0.1 g catalyst was added into the RhB aqueous solution (100 mL, 5 mg/L) in dark and stirred for 30 min to reach adsorption–desorption equilibrium. After that, the mixed solution was treated with UV–vis light irradiation (300 W Xe lamp) and ultrasonic (50 W, 40 kHz). Change the water every five minutes

to avoid the effects of temperature. A 4 mL solution was taken out every 20 min and centrifuged to remove the catalyst. The residual amount of RhB was recorded by the UV–vis spectrophotometer (Yoke, N6000, Shanghai, China) within the range of 300–800 nm.

2.3. Characterization

X-ray diffractometer (XRD) patterns were obtained to validate the phase purity and crystallinity of the powders on the XRD equipment (Rigaku Smartlab Beijing Co, Beijing, China). Scanning electron microscope (SEM) images of the prepared catalysts, including energy dispersive X-ray spectroscopy (EDS) capabilities, were measured with an SEM Regulus 8230, Hitachi Co, Tokyo, Japan. The transmission electron microscope (TEM) was used by JEOL JEM-F200 (Tokyo, Japan). The absorption spectra of these powders were tested in a UV-vis spectrophotometer (PerkinElmer Lambda 35, Waltham, MA, USA). X-ray photoelectron spectroscopy (XPS) was carried out with a ESCALAB 250, Thermo-VG Scientific, Waltham, MA, USA to analyze the components and the valence states. The specific surface areas of the samples were tested by Micromeritics ASAP 2460 Brunauer-Emmet-Teller (BET, Shanghai, China) equipment with N_2 as the carrier gas. The polarization electric field (P-E) loops and electric-field-induced strain (S-E) were tested in silicone oil at room temperature with 1 Hz frequency using a MultiFerroic II, Radiant technologies Inc., Albuquerque, New Mexico. The sample powders were pressed in a pellet (1 cm diameter and 0.20 mm thick) with Polyvinyl Alcohol (PVA) solution as a binder and then annealed at 600 °C to burn out the PVA binder. The pellets were coated on both sides with Au electrodes.

3. Results and Discussion

X-ray diffraction patterns (XRD) of BiOCl, $NaNbO_3$, and a series of BiOCl/$NaNbO_3$ piezoelectric composites are shown in Figure 1a. The distinct diffraction peaks of pure BiOCl can be related to tetragonal BiOCl (PDF card no. 82–0485, space group: P4/nmm), and the diffraction peaks of pure $NaNbO_3$ can be indexed to orthorhombic $NaNbO_3$ (PDF card no. 77–0873, space group: $P2_1ma$). As for BiOCl/$NaNbO_3$ piezoelectric composites (BN-1, BN-2, BN-3, BN-4), there are both BiOCl and $NaNbO_3$ peaks can be observed. In addition, the crystallite sizes were calculated by Scherrer formula: $D = \frac{K\lambda}{\beta cos\theta}$, where D is crystallite size (nm), K is 0.9 (Scherrer constant), λ is 0.15406 nm (wavelength of the X-ray sources). The average crystallite sizes of BiOCl, $NaNbO_3$, and BN-3 are 57, 22, and 56 nm. With the increase of $NaNbO_3$ content, the diffraction peaks increased. The UV–vis diffuse reflectance spectra (DRS) of BiOCl, $NaNbO_3$, and BN-3 are exhibited in Figure 1b, which indicate the absorbance threshold of $NaNbO_3$, BiOCl, and BN-3 are the same. The estimated band gaps (E_g) of BiOCl and $NaNbO_3$ are computed in Figure 1c by $(Ahv)^{2/n} \sim hv - E_g$, where A is for absorbance, hv is for irradiation energy [20], and the obtained values are 3.44 and 3.52 eV, respectively. The valance band X-ray photoelectron spectroscopy (VB XPS) spectra in Figure 1d show that the valance band values of BiOCl and $NaNbO_3$ are 2.57 and 2.50 eV. Together with the band gaps, the conductive band (CB) position can be calculated by $E_{VB} = E_{CB} - E_g$, which are −0.87 (BiOCl) and −1.02 eV ($NaNbO_3$).

The morphology and microstructure of the BN-3 powder were investigated by scanning electron microscopy (SEM), element mapping and transmission electron microscope (TEM), and the results were shown in Figure 2. From Figure 2a, the irregular particles can be observed and the distribution of the corresponding main elements are shown in Figure 2b–f. The different colored areas suggest that Nb-, Na-, O-, Bi-, and Cl-enriched areas of the BN-3 composite, respectively. The TEM image of the BN-3 powder is displayed in Figure 2g. The lattice spacing of 0.343 and 0.273 nm in Figure 2h–i are corresponding to the (101) of BiOCl and (121) plane of $NaNbO_3$, respectively. The result agrees well with that in the XRD patterns as shown in Figure 1a.

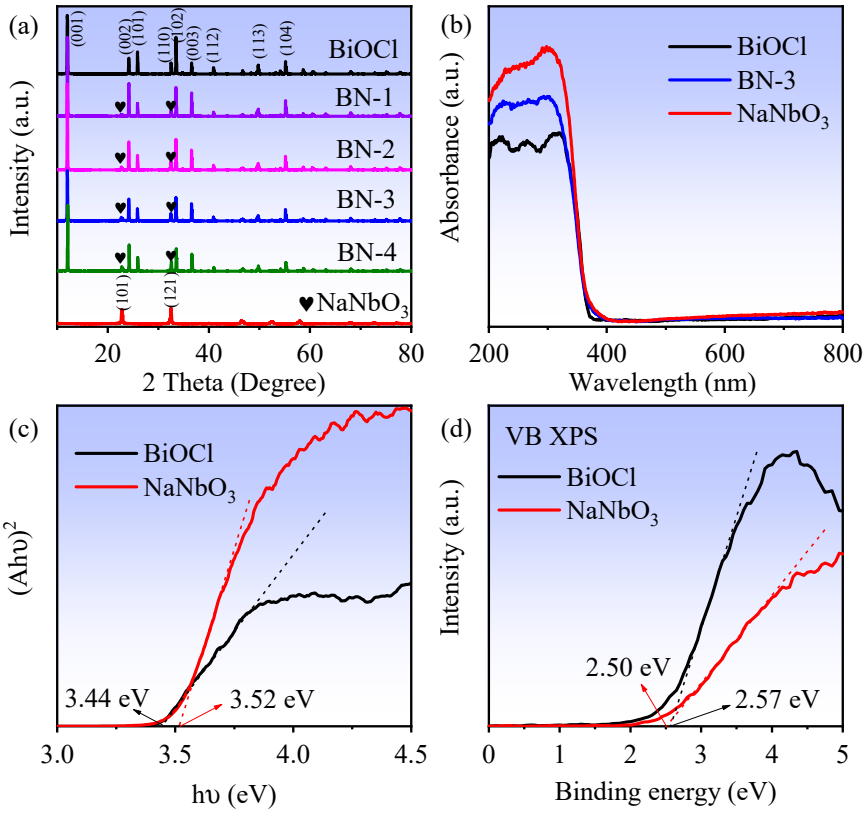

Figure 1. (**a**) XRD patterns of BiOCl, $NaNbO_3$, and BiOCl/$NaNbO_3$ piezoelectric composites; (**b**) UV–vis absorption spectra; (**c**) the estimated band gaps of BiOCl and $NaNbO_3$; (**d**) VB XPS spectra of BiOCl and $NaNbO_3$.

X-ray photoelectron spectroscopy (XPS) spectra of the BiOCl, $NaNbO_3$, and BN-3 piezoelectric composite are shown in Figure 3. From Figure 3a, the peaks of Bi 4f of BiOCl (BN-3) located at 159.60 (159.24 eV) and 164.90 eV (164.52 eV) can be assigned to Bi $4f_{7/2}$ and Bi $4f_{5/2}$, respectively, suggesting the Bi^{3+} exists in the BiOCl (BN-3). In Figure 3b, the Cl 2p peaks at 198.29 (197.90 eV) and 199.93 eV (199.54 eV) can be attributed to Cl $2p_{3/2}$ and Cl $2p_{1/2}$, respectively, which indicate the Cl^- in BiOCl (BN-3) [21]. The peak at 1070.62 eV (1071.42 eV) in Figure 3c is ascribed to Na 1s in $NaNbO_3$ (BN-3). In Figure 3d, it is clearly seen that the binding energies located at 206.67 (207.05 eV) and 209.40 eV (209.78 eV) belong to Nb $3d_{5/2}$ and Nb $3d_{3/2}$, respectively, reflecting that Nb is in the Nb (+5) chemical state [22]. As shown in Figure 3e, the peaks located at 530.39 (BiOCl), 529.60 ($NaNbO_3$), and 529.98 eV (BN-3) correspond to O 1s. Compared with BiOCl, the blue shift of all peaks for BN-3 can be observed, while the red shift compared with $NaNbO_3$. The XPS survey spectra also indicate that BiOCl is composed of Bi, O, and Cl elements, and $NaNbO_3$ is mainly composed of Na, O, and Nb elements, while BN-3 contains all elements above, as shown in Figure 3f. In short, the XPS results demonstrate that the BN-3 piezoelectric composite is composed of BiOCl and $NaNbO_3$.

The polarization electric field hysteresis loop (P-E) and electric-field-induced strain (S-E) curves of BN-3 composite are displayed in Figure 4. From Figure 4a, a saturated and nearly squared P-E loop can be observed, and the remnant polarization (Pr) is 35.13 $\mu C/cm^2$ and the coercive field (Ec) is 8.72 kV/mm. The result shows that BN-3 composite has well ferroelectric properties, favoring the spatial separation and transportation of photo-induced carriers [23]. The S-E curve in Figure 4b exhibits an asymmetric butterfly shape, confirming the piezoelectricity of the BN-3 composite [24,25].

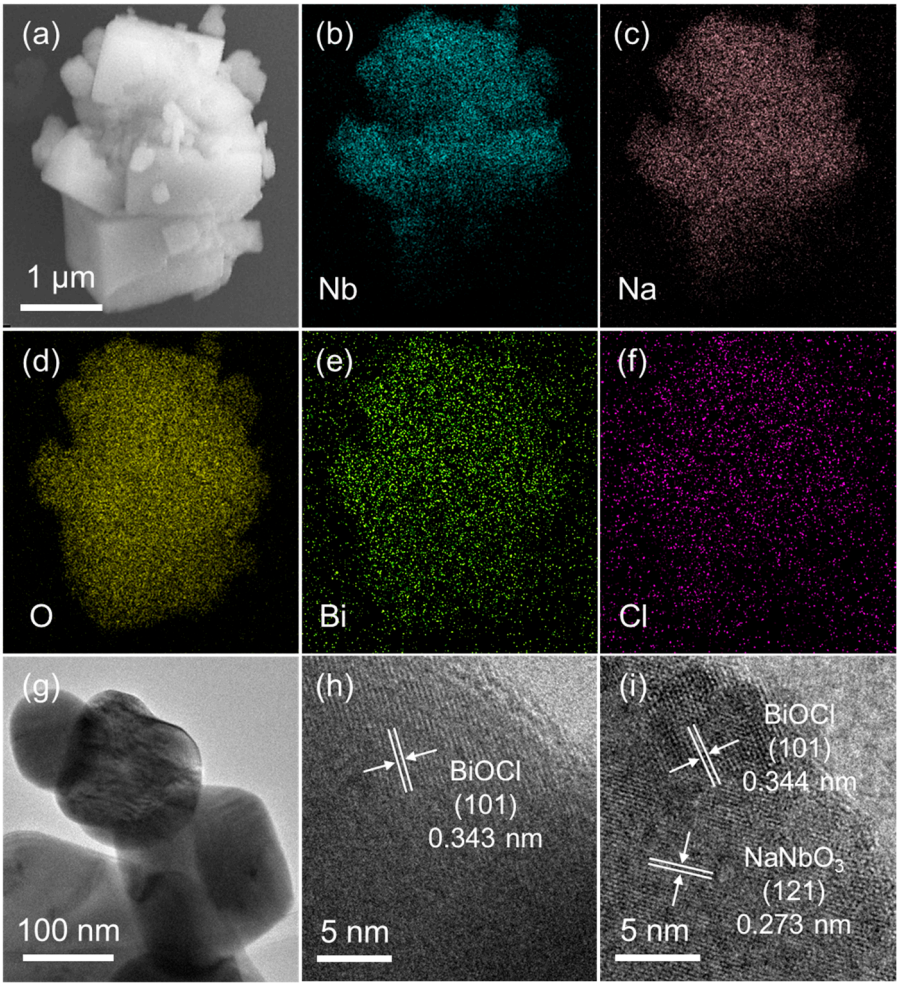

Figure 2. (**a**) SEM image; (**b**–**f**) EDS element mappings; (**g**) TEM image; (**h**,**i**) lattice fringes images of BN-3.

Consequently, the piezo/photocatalytic activities of BiOCl, $NaNbO_3$, and BiOCl/$NaNbO_3$ piezoelectric composites were evaluated by the degradation of Rhodamine B (RhB) under the condition of light irradiation and ultrasound. From Figure 5a, BN-3 exhibits better piezo/photocatalytic performance than that of BiOCl, $NaNbO_3$, and other content BiOCl/$NaNbO_3$ composites. The rate constant k values are obtained from Figure 5a via the pseudo-first-order equation [26]: $\ln(C_0/C_t) = -kt$, where C_0 is RhB concentration for initial and C_t is for after irradiation time t. And the decomposition ratio is calculated via the formula: $\eta = \left(1 - \frac{C_t}{C_0}\right) \times 100\%$. As shown in Figure 5b, the apparent reaction rate constant k for BiOCl, BN-1, BN-2, BN-3, BN-4, and $NaNbO_3$ is 0.0089, 0.0112, 0.0134, 0.0192, 0.0168, and 0.0037 min^{-1}, respectively. The piezo/photodegradation rate of RhB for BN-3 is 2.2 and 5.2 times higher than that of BiOCl and $NaNbO_3$, the histogram in Figure 5c reflects this directly. The degradation percentages of BiOCl, $NaNbO_3$ and BN-3 are 29.8%, 61.9% and 87.4%, respectively. In addition, the BET surface areas of BiOCl, $NaNbO_3$, and BN-3 are 0.24, 2.00, and 1.32 m^2/g, and the pore volumes are 0.0008, 0.0088, and 0.0037 cm^3/g, respectively. The BET surface areas of the samples are in the same order of magnitude, which means the BET surface areas not can decisive the catalytic activity. This result indicates the heterojunction in BN-3 exerts a tremendous advantage on the piezo/photocatalytic process. To investigate the most reactive species during the process of RhB decomposition, the radical trapping experiments were carried out in the presence of BN-3 as a catalyst. From Figure 5d, the piezo-photodegradation efficiency of RhB is remarkably inhibited while adding the triethanolamine (TEOA, 50 μL) scavenger for

trapping hole (h^+) to the mixed solution, demonstrating an important role of h^+ in the piezo-photocatalytic process. While L-ascorbic acid (VC, 40 mg) for superoxide radical ($\cdot O_2^-$) was added, the degradation efficiency also decreased rapidly. The RhB degradation efficiency is decreased slightly by adding the isopropanol (IPA, 50 μL), reflecting the hydroxyl radical (·OH) plays a secondary role in this process. These results indicate that the effect in this piezo-photocatalytic process is: $h^+ > \cdot O_2^- > \cdot OH$.

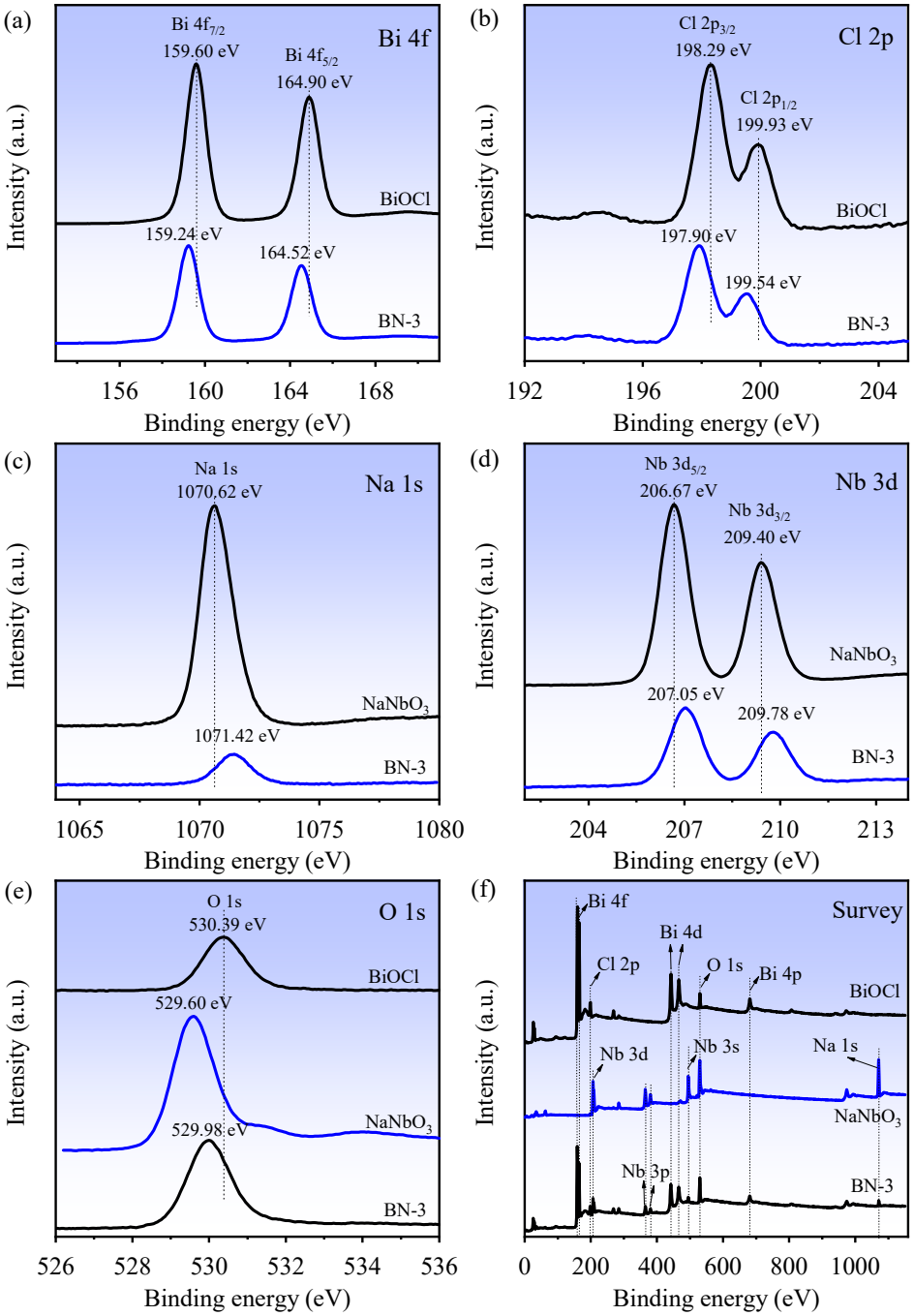

Figure 3. XPS survey spectra of BiOCl, $NaNbO_3$, and BN-3: (**a**) Bi 4f; (**b**) Cl 2p; (**c**) Na 1s; (**d**) Nb 3d; (**e**) O 1s; (**f**) Survey.

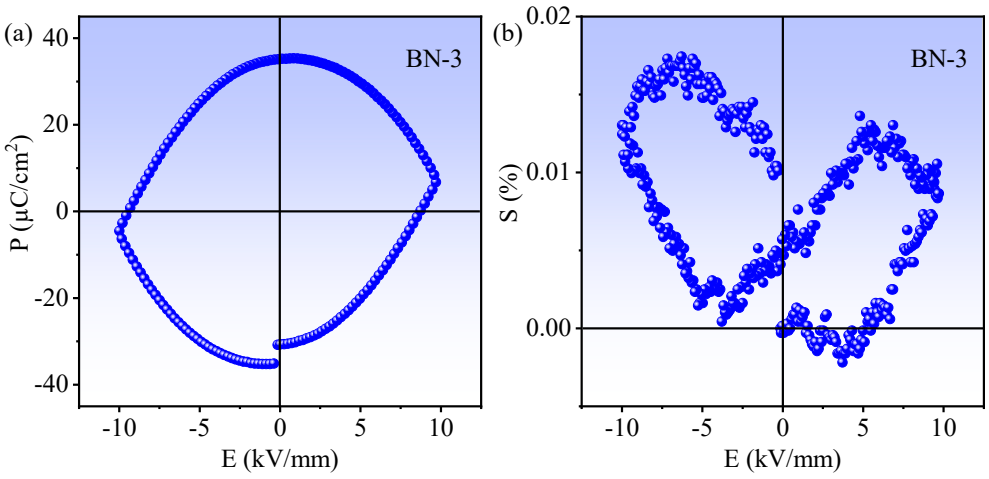

Figure 4. (**a**) The ferroelectric P-E loop and (**b**) electric field-induced S-E curve of BN-3 composite.

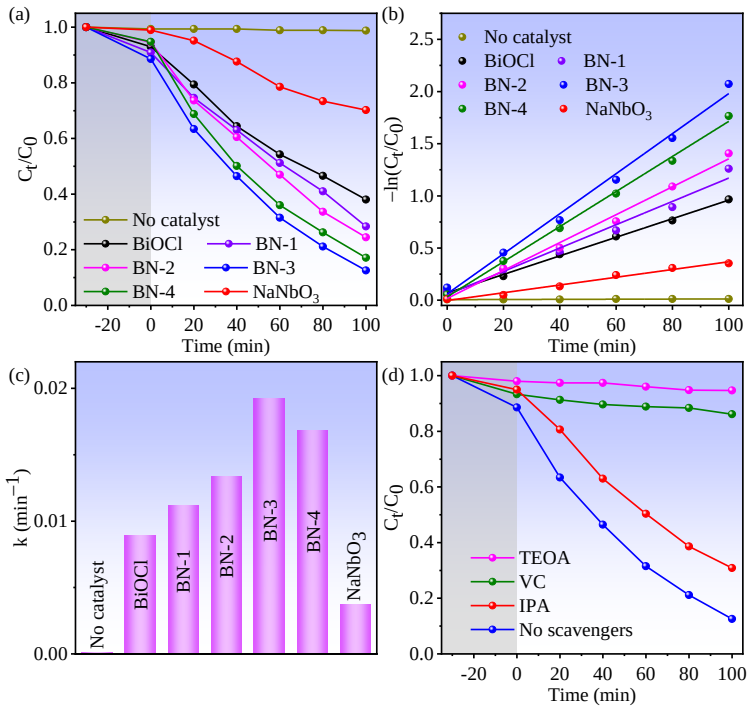

Figure 5. (**a**) The kinetic curves of piezo-photodegradation RhB performance for BiOCl, $NaNbO_3$, and BiOCl/$NaNbO_3$ piezoelectric composites; (**b**) the dynamics of degradation reaction [$(-\ln(C_t/C_0)]$; (**c**) the histogram of corresponding reaction rate constant; (**d**) piezo-photodegradation curves with disparate scavengers of BN-3 composite.

To demonstrate the piezocatalysis, photocatalysis, and the synergy effect of piezocatalysis and photocatalysis of BN-3 piezoelectric composite, the RhB degradation capability within 100 min was measured under the condition of ultrasound only, light only, and ultrasound + light together. UV–vis absorption spectra of RhB for BN-3 under different conditions are shown in Figure 6a,c,e, which correspond to light, ultrasound, and both light and ultrasound, respectively. From Figure 6b,d,f, the degradation rate is the lowest under the condition of only ultrasound, the rate constant k (0.0005 min^{-1}) and decomposition ratio (9.9%) are well below those of the condition of only light (0.0044 min^{-1} and 40.4%) and light + ultrasound together (0.0192 min^{-1} and 87.4%). The decomposition ratio of RhB under synergy of piezocatalysis and photocatalysis is 8.8 and 2.2 times higher than that of piezocatalysis and photocatalysis, respectively. The rate constant k under synergy of

piezocatalysis and photocatalysis is 38.4 and 4.36 times higher than that of only ultrasound and only light. In addition, based on the same condition, compared to other piezoelectric materials past reported, the k value of BN-3 is higher than that of $NaNbO_3/CuBi_2O_4$ nanocomposites (0.0112 min^{-1}) [27], and closing to that of $BaTiO_3/KNbO_3$ heterostructure (0.01492 min^{-1}) [28]. The result confirms that the synergy effect of piezocatalysis and photocatalysis of $BiOCl/NaNbO_3$ piezoelectric composite plays an important role in the highly efficient degradation of RhB. One of the key parameters in the piezo-photocatalyst is reproducibility, and Figure 7 shows the cycling performance of the piezo-photocatalytic activity of BN-3 for degrading RhB. After three cycles, the degradation efficiency is just reduced a little. This result evidences that BN-3 possesses a high reproducibility.

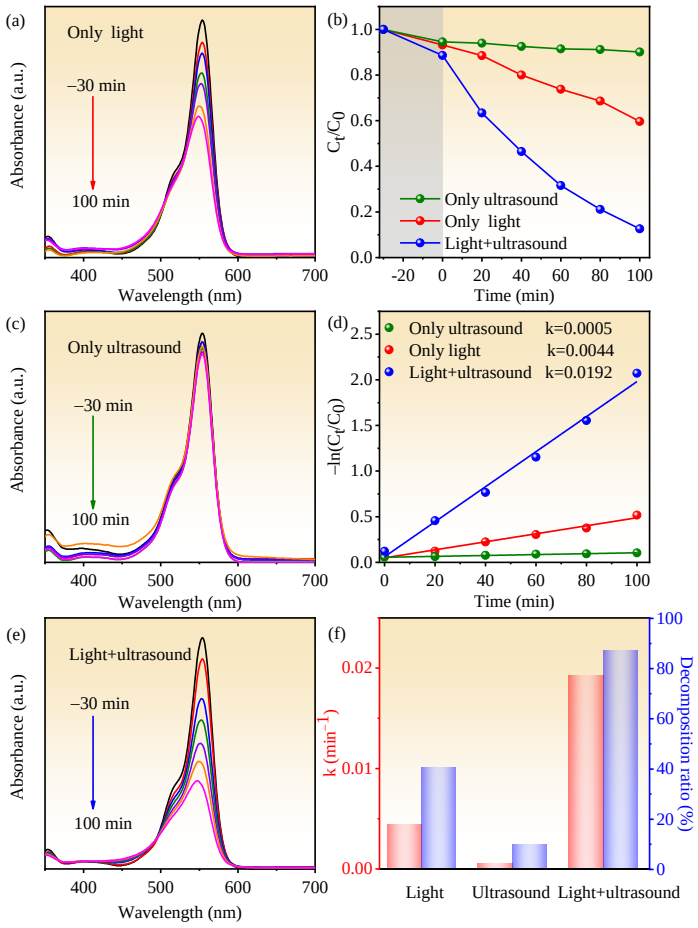

Figure 6. UV–vis spectral absorption of RhB for BN-3 under the condition of (**a**) only light, (**c**) only ultrasound and (**e**) light + ultrasound; (**b**) the kinetic curves of RhB degradation for BN-3 under these three control conditions; (**d**) the dynamics of degradation reaction [$(-\ln(C_t/C_0)]$; (**f**) the histogram of corresponding reaction rate constant and decomposition ratio.

On the basis of the above analysis, the possible mechanism for piezocatalytic, photocatalytic, and their synergetic catalytic process of $BiOCl/NaNbO_3$ piezoelectric composites are shown in Figure 8. According to our experiment, the valance band of $NaNbO_3$ is 2.50 eV, while BiOCl is 2.57 eV; the conductive band of $NaNbO_3$ is −1.02 eV, while BiOCl is −0.87 eV. In the condition of only light, the photoelectrons are excited from the valance band to the conductive band, and the electrons will transfer from the conductive band of $NaNbO_3$ to the conductive band of BiOCl, and thus build an inner electric field. The built-in electric field can promote the separation of electrons and holes. However, there is still a combination of electrons and holes in the inner of $BiOCl/NaNbO_3$ piezoelectric composites because the built-in electric field is easily prone to be screened by electrostatic compensated free space charges [29]. This reduces the degradation efficiency of RhB. In

the condition of only ultrasound, the cavitation bubbles will form, expand, and burst, an amount of electric charge can be generated [30,31]. These positive and negative charges will transfer to the opposite directions under the influence of the alternating built-in electric field. In the condition of both light and ultrasound, the electrons and holes located at the conductive band and valance band will transfer to the opposite directions under the internal piezoelectric potential, causing electrons to accumulate in the conductive band of BiOCl and holes accumulate in the valance band of $NaNbO_3$ [32–34]. Subsequently, the electrons on the CB of BiOCl combined with the absorbed O_2 to produce $\cdot O_2^-$. Meanwhile, part holes on the VB of $NaNbO_3$ will oxidize hydroxyl to form ·OH. Finally, the reactive species ·OH, h^+, and $\cdot O_2^-$ will participate in the oxidative degradation of RhB. The combination rate of electrons and holes will be reduced significantly under the built-in electric field, thus the decomposition ratio of $BiOCl/NaNbO_3$ piezoelectric composite increased remarkably.

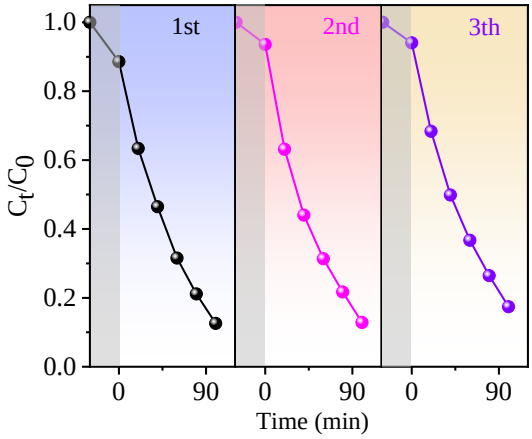

Figure 7. The cycling performance of the piezo-photocatalytic activity of BN-3 for degrading RhB solution.

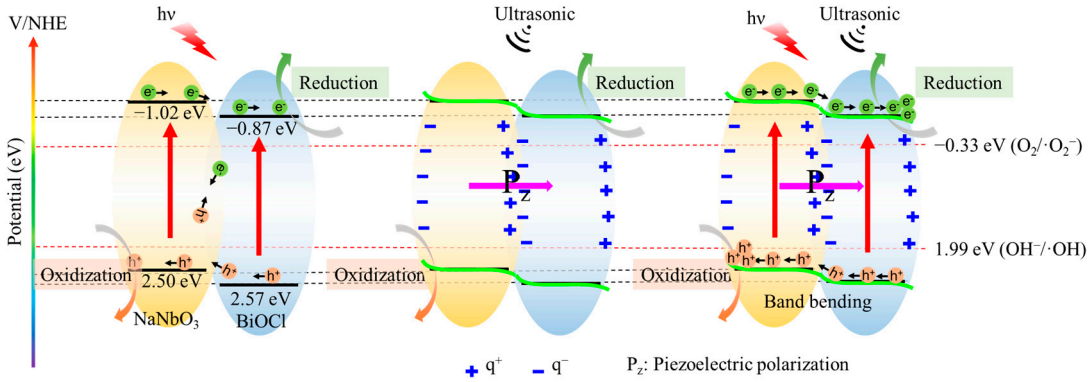

Figure 8. Possible piezocatalytic, photocatalytic, and piezo-photocatalytic mechanism of $BiOCl/NaNbO_3$ piezoelectric composites.

4. Conclusions

In conclusion, $BiOCl/NaNbO_3$ piezoelectric composites are synthesized via a two-step hydrothermal route. Under UV–vis light and ultrasonic exposure, the BN-3 for piezo-photocatalytic decomposition of RhB demonstrate remarkable piezo-photocatalytic performance than that of BiOCl and $NaNbO_3$ component due to the heterojunction construction. Furthermore, the piezo/photodegradation rate of RhB for BN-3 is higher than that of piezocatalysis and photocatalysis, indicating the synergistic effect of piezocatalysis and photocatalysis plays a significant role in the degradation process. Some issues, such as the specific promotion mechanism of the $NaNbO_3$ and BiOCl of the contribution of the piezo-photocatalytic performance, need to be further investigated for better understand-

ing. However, this work provides a feasible approach for the development of efficient piezoelectric photocatalysts for heterojunction construction.

Author Contributions: Conceptualization, C.W. and F.L.; methodology, C.W.; investigation, L.L.; resources, C.W. and F.L.; data curation, L.L.; software, L.L.; W.C., J.Y. and W.L.; writing original draft preparation, L.L.; writing review and editing, L.L., C.W. and F.L.; supervision, C.W. and F.L. All authors have read and agreed to the published version of the manuscript.

Funding: This work was financially supported by the National Natural Science Foundation of China (Grant Nos. 12174001, 12104001, and 51872001).

Data Availability Statement: Data available in a publicly accessible repository. The data presented in this study are openly available in [repository name e.g., FigShare] at [doi], reference number [reference number].

Conflicts of Interest: The authors declare no conflict of interest.

References

1. Hu, L.; Yang, S.; Zhao, Y.; He, J.; Jiang, S.; Sun, C.; Song, S. Spontaneous polarization electric field briskly boosting charge separation and transfer for sustainable photocatalytic H_2 bubble evolution. *Appl. Catal. B* **2021**, *283*, 119631. [CrossRef]
2. Wang, Y.C.; Wu, J.M. Effect of controlled oxygen vacancy on H_2-production through the piezocatalysis and piezophototronics of ferroelectric R3C $ZnSnO_3$ nanowires. *Adv. Funct. Mater.* **2019**, *30*, 1907619. [CrossRef]
3. El-Bindary, A.A.; El-Marsafy, S.M.; El-Maddah, A.A. Enhancement of the photocatalytic activity of ZnO nanoparticles by silver doping for the degradation of AY99 contaminants. *J. Mol. Struct.* **2019**, *1191*, 76–84. [CrossRef]
4. Kiwaan, H.A.; Atwee, T.M.; Azab, E.A.; El-Bindary, A.A. Efficient photocatalytic degradation of Acid Red 57 using synthesized ZnO nanowires. *J. Chin. Chem. Soc.* **2019**, *66*, 89–98. [CrossRef]
5. Wang, Y.; Cai, J.; Wu, M.; Chen, J.; Zhao, W.; Tian, Y.; Ding, T.; Zhang, J.; Jiang, Z.; Li, X. Rational construction of oxygen vacancies onto tungsten trioxide to improve visible light photocatalytic water oxidation reaction. *Appl. Catal. B* **2018**, *239*, 398–407. [CrossRef]
6. Ye, L.; Zan, L.; Tian, L.; Peng, T.; Zhang, J. The {001} facets-dependent high photoactivity of BiOCl nanosheets. *Chem. Commun.* **2011**, *47*, 6951–6953. [CrossRef]
7. Li, Q.; Guan, Z.; Wu, D.; Zhao, X.; Bao, S.; Tian, B.; Zhang, J. Z-scheme BiOCl-Au-CdS heterostructure with enhanced sunlight-driven photocatalytic activity in degrading water dyes and antibiotics. *ACS Sustain. Chem. Eng.* **2017**, *5*, 6958–6968. [CrossRef]
8. Li, T.B.; Chen, G.; Zhou, C.; Shen, Z.Y.; Jin, R.C.; Sun, J.X. New photocatalyst BiOCl/BiOI composites with highly enhanced visible light photocatalytic performances. *Dalton Trans.* **2011**, *40*, 6751–6758. [CrossRef]
9. Yang, Y.; Zhang, C.; Lai, C.; Zeng, G.; Huang, D.; Cheng, M.; Wang, J.; Chen, F.; Zhou, C.; Xiong, W. BiOX (X=Cl, Br, I) photocatalytic nanomaterials: Applications for fuels and environmental management. *Adv. Colloid Interface Sci.* **2018**, *254*, 76–93. [CrossRef]
10. Yuan, B.; Wu, J.; Qin, N.; Lin, E.; Bao, D. Enhanced piezocatalytic performance of (Ba,Sr)TiO_3 nanowires to degrade organic pollutants. *ACS Appl. Nano Mater.* **2018**, *1*, 5119–5127. [CrossRef]
11. Liu, X.; Xiao, L.; Zhang, Y.; Sun, H. Significantly enhanced piezo-photocatalytic capability in $BaTiO_3$ nanowires for degrading organic dye. *J. Materiomics* **2020**, *6*, 256–262. [CrossRef]
12. Li, L.; Ma, Y.; Chen, G.; Wang, J.; Wang, C. Oxygen-vacancy-enhanced piezo-photocatalytic performance of AgNbO. *Scr. Mater.* **2022**, *206*, 114234. [CrossRef]
13. Lei, H.; Zhang, H.; Zou, Y.; Dong, X.; Jia, Y.; Wang, F. Synergetic photocatalysis/piezocatalysis of bismuth oxybromide for degradation of organic pollutants. *J. Alloys Compd.* **2019**, *809*, 151840. [CrossRef]
14. Zhou, X.; Wu, S.; Li, C.; Yan, F.; Bai, H.; Shen, B.; Zeng, H.; Zhai, J. Piezophototronic effect in enhancing charge carrier separation and transfer in ZnO/$BaTiO_3$ heterostructures for high-efficiency catalytic oxidation. *Nano Energy* **2019**, *66*, 104127. [CrossRef]
15. Singh, S.; Khare, N. Coupling of piezoelectric, semiconducting and photoexcitation properties in $NaNbO_3$ nanostructures for controlling electrical transport: Realizing an efficient piezo-photoanode and piezo-photocatalyst. *Nano Energy* **2017**, *38*, 335–341. [CrossRef]
16. Ma, J.; Jia, Y.; Chen, L.; Zheng, Y.; Wu, Z.; Luo, W.; Jiang, M.; Cui, X.; Li, Y. Dye wastewater treatment driven by cyclically heating/cooling the poled $(K_{0.5}Na_{0.5})NbO_3$ pyroelectric crystal catalyst. *J. Clean. Prod.* **2020**, *276*, 124218. [CrossRef]
17. Zhang, A.; Liu, Z.; Geng, X.; Song, W.; Lu, J.; Xie, B.; Ke, S.; Shu, L. Ultrasonic vibration driven piezocatalytic activity of lead-free $K_{0.5}Na_{0.5}NbO_3$ materials. *Ceram. Int.* **2019**, *45*, 22486–22492. [CrossRef]
18. You, H.; Ma, X.; Wu, Z.; Fei, L.; Chen, X.; Yang, J.; Liu, Y.; Jia, Y.; Li, H.; Wang, F.; et al. Piezoelectrically/pyroelectrically-driven vibration/cold-hot energy harvesting for mechano-/pyro- bi-catalytic dye decomposition of $NaNbO_3$ nanofibers. *Nano Energy* **2018**, *52*, 351–359. [CrossRef]
19. Ismail, M.; Wu, Z.; Zhang, L.; Ma, J.; Jia, Y.; Hu, Y.; Wang, Y. High-efficient synergy of piezocatalysis and photocatalysis in bismuth oxychloride nanomaterial for dye decomposition. *Chemosphere* **2019**, *228*, 212–218. [CrossRef] [PubMed]

20. Kamat, P.V. Photochemistry on Nonreactive and Reactive (Semiconductor) Surfaces. *Chem. Rev.* **1993**, *93*, 267–300. [CrossRef]
21. Pan, J.; Liu, J.; Zuo, S.; Khan, U.A.; Yu, Y.; Li, B. Structure of Z-scheme CdS/CQDs/BiOCl heterojunction with enhanced photocatalytic activity for environmental pollutant elimination. *Appl. Surf. Sci.* **2018**, *444*, 177–186. [CrossRef]
22. Liu, Q.; Chai, Y.; Zhang, L.; Ren, J.; Dai, W.L. Highly efficient Pt/$NaNbO_3$ nanowire photocatalyst: Its morphology effect and application in water purification and H_2 production. *Appl. Catal. B* **2017**, *205*, 505–513. [CrossRef]
23. Yu, Z.; Zhan, B.; Ge, B.; Zhu, Y.; Dai, Y.; Zhou, G.; Yu, F.; Wang, P.; Huang, B.; Zhan, J. Synthesis of high efficient and stable plasmonic photocatalyst Ag/$AgNbO_3$ with specific exposed crystal–facets and intimate heterogeneous interface via combustion route. *Appl. Surf. Sci.* **2019**, *488*, 485–493. [CrossRef]
24. Liu, L.; Shi, D.; Knapp, M.; Ehrenberg, H.; Fang, L.; Chen, J. Large strain response based on relaxor–antiferroelectric coherence in $Bi_{0.5}Na_{0.5}TiO_3$–$SrTiO_3$–$(K_{0.5}Na_{0.5})NbO_3$ solid solutions. *J. Appl. Phys.* **2014**, *116*, 184104. [CrossRef]
25. Zhu, M.; Li, S.; Zhang, H.; Gao, J.; Kwok, K.W.; Jia, Y.; Kong, L.B.; Zhou, W.; Peng, B. Diffused phase transition boosted dye degradation with Ba $(Zr_xTi_{1-x})O_3$ solid solutions through piezoelectric effect. *Nano Energy* **2021**, *89*, 106474. [CrossRef]
26. Turchi, C.S.; Ollis, D.F. Photocatalytic degradation of organic water contaminants: Mechanisms involving hydroxyl radical attack. *J. Catal.* **1990**, *122*, 178–192. [CrossRef]
27. Rajan, K.D.; Gotipamul, P.P.; Khanna, S.; Chidambaram, S.; Rathinam, M. Piezo-photocatalytic effect of $NaNbO_3$ interconnected nanoparticles decorated $CuBi_2O_4$ nanocuboids. *Mater. Lett.* **2021**, *296*, 129902. [CrossRef]
28. Zhang, Y.; Shen, G.; Sheng, C.; Zhang, F.; Fan, W. The effect of piezo-photocatalysis on enhancing the charge carrier separation in $BaTiO_3$/$KNbO_3$ heterostructure photocatalyst. *Appl. Surf. Sci.* **2021**, *562*, 150164. [CrossRef]
29. Li, H.; Sang, Y.; Chang, S.; Huang, X.; Zhang, Y.; Yang, R.; Jiang, H.; Liu, H.; Wang, Z.L. Enhanced ferroelectric–nanocrystal–based hybrid photocatalysis by ultrasonic–wave–generated piezophototronic effect. *Nano Lett.* **2015**, *15*, 2372–2379. [CrossRef]
30. Hu, C.; Huang, H.; Chen, F.; Zhang, Y.; Yu, H.; Ma, T. Coupling piezocatalysis and photocatalysis in Bi_4NbO_8X (X = Cl, Br) polar single crystals. *Adv. Funct. Mater.* **2019**, *30*, 1908168. [CrossRef]
31. Sharma, M.; Halder, A.; Vaish, R. Effect of Ce on piezo/photocatalytic effects of $Ba_{0.9}Ca_{0.1}Ce_xTi_{1-x}O_3$ ceramics for dye/ pharmaceutical waste water treatment. *Mater. Res. Bull.* **2020**, *122*, 110647. [CrossRef]
32. Zhao, T.; Wang, Q.; Du, A. High piezo–photocatalytic efficiency of H_2 production by CuS/ZnO nanostructure under solar and ultrasonic exposure. *Mater. Lett.* **2021**, *294*, 129752. [CrossRef]
33. Yang, B.; Chen, H.; Yang, Y.; Wang, L.; Bian, J.; Liu, Q.; Lou, X. Insights into the tribo–/pyro–catalysis using Sr–doped $BaTiO_3$ ferroelectric nanocrystals for efficient water remediation. *Chem. Eng. J.* **2021**, *416*, 128986. [CrossRef]
34. Zhou, X.; Yan, F.; Wu, S.; Shen, B.; Zeng, H.; Zhai, J. Remarkable piezophoto coupling catalysis behavior of BiOX/$BaTiO_3$ (X = Cl, Br, $Cl_{0.166}Br_{0.834}$) piezoelectric composites. *Small* **2020**, *16*, 2001573. [CrossRef] [PubMed]